



# Support effect in Co<sub>3</sub>O<sub>4</sub>-based catalysts for selective partial oxidation of glycerol to lactic acid

Sebastian Torres, Ruben Palacio, Diana López \*

Química de Recursos Energéticos y Medio Ambiente, Instituto de Química, Facultad de Ciencias Exactas y Naturales, Universidad de Antioquia UdeA, Calle 70 No. 52-21, Medellín, Colombia

## ARTICLE INFO

**Keywords:**  
Metal oxides  
Spinel Co<sub>3</sub>O<sub>4</sub>  
Lactic acid  
Glycerol  
Alcohol valorization

## ABSTRACT

Co<sub>3</sub>O<sub>4</sub> supported on CeO<sub>2</sub>, ZrO<sub>2</sub> and TiO<sub>2</sub>, were used as catalysts in glycerol partial oxidation to lactic acid. The aim was to establish the influence of the support on the cobalt-derived catalysts activity. The most active catalyst based on TOF followed the order: Co<sub>3</sub>O<sub>4</sub>/CeO<sub>2</sub> ( $1.2 \times 10^{-1} \text{ s}^{-1}$ ) > Co<sub>3</sub>O<sub>4</sub>/ZrO<sub>2</sub> ( $8.3 \times 10^{-2} \text{ s}^{-1}$ ) > Co<sub>3</sub>O<sub>4</sub>/TiO<sub>2</sub> ( $3.0 \times 10^{-2} \text{ s}^{-1}$ ), with lactic acid selectivity at comparable glycerol conversion ( $53.5 \pm 5.5 \%$ ) being higher when using CeO<sub>2</sub> support, Co<sub>3</sub>O<sub>4</sub>/CeO<sub>2</sub> (90 %) > Co<sub>3</sub>O<sub>4</sub>/ZrO<sub>2</sub> (78 %) > Co<sub>3</sub>O<sub>4</sub>/TiO<sub>2</sub> (68 %). These results indicated that the support type not only influenced activity but also selectivity to lactic acid. The Co<sub>3</sub>O<sub>4</sub>/CeO<sub>2</sub> catalyst with less exposed cobalt species at the surface enriched in Co<sup>3+</sup> ions, a more homogeneous composition of cobalt species being reduced at low temperatures, with acid sites of middle strength and lower density of acidic sites, is at the origin of a greater selectivity towards lactic acid, in addition this catalyst was active in 4 catalytic cycles.

## 1. Introduction

Biomass valorization for obtaining chemicals and fuels has gained a tremendous attention in the past three decades, especially because of the depletion of fossil fuels and the increase of the emissions of environmental harmful pollutants from combustion engines and industrial chemical activities. Biomass-derived chemicals and fuels is fundamental for reaching a more sustainable chemical industry, reduce harmful emissions and to achieve the sustainable development goals of the United Nations. The selective production of chemicals and fuels from biomass or its derivatives required the fine tuning of heterogeneous catalysts for achieving the desired molecules at high reaction rates, while being stable and recyclable [1–3]. Catalytic processes accounts for nearly 95 % in volume of the worldwide chemical-derived manufactured products [4], it is reported that heterogeneous catalysts account for nearly 90 % of all chemical processes [1] and are expected to play a key role in the development of new industrial chemical sustainable activities.

In general, most studied heterogeneous catalysts in biomass-derived chemical transformations are based on supported noble metals - Pt, Pd, Ir, Ru or Rh - for example, in hydrodeoxygenation reactions [5–7] or alcohol valorization [8–12]. In recent years, most attention has been paid to supported non-noble metals such as Ni [6,7,13–16] and Cu

[17–20]. Alcohol oxidation is an important reaction for producing aldehydes and carboxylic acids, these compounds are key intermediates in organic synthesis for obtaining valuable chemicals [9,21,22]. The development of heterogeneous catalysts based on transition metals is gaining more attention because of the low reserves of noble metals. Glycerol is a byproduct generated during biodiesel production, nearly 100 kg are produced per ton of biodiesel (10 wt%) [23], generating a global oversupply for instance, it is a drawback of the biodiesel industry and tremendous scientific efforts have been undertaken for finding practical applications. For decades, transformation of glycerol has been studied in an attempt to produce valuable chemicals [23–27]. Because of the high number of heterogeneous catalysts studied and reaction conditions analyzed, glycerol reactivity might be used as a *model reaction* for developing transition metal-based heterogeneous catalysts. Besides, biodiesel production will continue to increase in the next decades creating the need for efficient heterogeneous catalytic processes for transforming glycerol [23].

Organic acids are of significant importance in industrial chemistry [21]. One of the most important products that can be obtained from glycerol is lactic acid, since it is a chemical platform for the synthesis of various chemical intermediates and biodegradable polymers [22, 27–29]. Copper- [17–20,30,31], nickel- [16,32,33], and bimetallic NiCo- [32], AuCu- [34,35], PtRu- [12], AuPt- [12,36] based catalysts

\* Corresponding author.

E-mail address: [diana.lopez@udea.edu.co](mailto:diana.lopez@udea.edu.co) (D. López).

<https://doi.org/10.1016/j.apcata.2021.118199>

Received 3 October 2020; Received in revised form 21 April 2021; Accepted 28 April 2021

Available online 30 April 2021

0926-860X/© 2021 Elsevier B.V. All rights reserved.

have been widely studied for converting glycerol to lactic acid at moderate reaction temperatures at different NaOH/glycerol mole ratio. More recently, cobalt-based catalysts have also received attention for selectively transforming glycerol into different chemicals [37,38]. Cerium oxide supported  $\text{Co}_3\text{O}_4$  particles is reported to be active in the selective conversion of glycerol to lactic acid in aqueous medium and basic pH at 250 °C, reaching a selectivity of 79.8 % with a conversion of 85.7 % [38]. Nevertheless, the catalyst exhibited low stability under cycling. It is worth noting that it is unknown which species of cobalt are more active and what is the effect of the support on the catalytic properties of  $\text{Co}_3\text{O}_4$  particles in the partial oxidation reaction of glycerol to lactic acid. Therefore, in order to determine the potential of these catalysts in the selective conversion of glycerol to lactic acid, it is necessary to continue the development and physicochemical characterization.

In this work, spinel-like cobalt oxide particles are supported in three different supports but with similar textural properties: cerium oxide, zirconium oxide, and titanium oxide.  $\text{Co}_3\text{O}_4$  is stable under basic conditions as well as  $\text{CeO}_2$ ,  $\text{ZrO}_2$  and  $\text{TiO}_2$ . The aim is to determine the influence of the support chemical properties in terms of acidity and redox properties on spinel-like cobalt oxide species and to determine the activity and stability of these catalysts in glycerol selective conversion to lactic acid.

## 2. Experimental

### 2.1. Supports preparation

#### 2.1.1. $\text{CeO}_2$ synthesis

$\text{CeO}_2$  was prepared by hydrothermal treatment of a solution containing 9 g of  $\text{Ce}(\text{NO}_3)_3 \cdot 6\text{H}_2\text{O}$  dissolved in 240 mL of ultrapure  $\text{H}_2\text{O}$  and 19 g of NaOH (NaOH:Ce molar ratio of 23) at 100 °C for 14 h [38].

#### 2.1.2. $\text{ZrO}_2$ synthesis

150 mL of a 2.5 M NaOH solution was added dropwise to a solution containing 9 g of  $\text{ZrO}(\text{NO}_3)_2 \cdot \text{XH}_2\text{O}$  dissolved in 150 mL of ultrapure  $\text{H}_2\text{O}$  [39]. The resulting mixture was stirred for 30 min and then it was transferred to an autoclave for a hydrothermal synthesis at 170 °C for 5 h.

#### 2.1.3. $\text{TiO}_2$ synthesis

10 mL of titanium isopropoxide (TTIP) was mixed with 15 mL of ethanol, then 15 mL of ultrapure  $\text{H}_2\text{O}$  was added dropwise and the resulting mixture was stirred for 2 h at room temperature [40], then the mixture was transferred into an autoclave and heated at 80 °C for 4 h. Finally, the recovered solid was calcined at 400 °C for 4 h.

### 2.2. Catalysts preparation

3 g of support was dispersed in 10 mL of ultrapure  $\text{H}_2\text{O}$  and then a solution of  $\text{Co}(\text{NO}_3)_2 \cdot 6\text{H}_2\text{O}$  containing the required amount for the desired cobalt loading (20 wt%) was added dropwise. The resulting mixture was stirred for 1 h at room temperature, followed by a slow evaporation of the solvent at 50 °C under stirring. Then, the solid was further dried at 50 °C in a vacuum oven and finally calcined in air at 400 °C during 4 h, with a heating rate of 2 °C  $\text{min}^{-1}$ .

### 2.3. Characterization of catalysts

The experimental content of cobalt in the catalysts was determined by atomic emission spectroscopy using a 4200 MP-AES Agilent technologies spectrophotometer, equipped with a CCD detector, wavelength of 340.512 nm for cobalt. For analysis, 3 mg of powder was dissolved in *aqua regia* (HCl :  $\text{HNO}_3$  volume ratio 3 : 1) and HF.

Nitrogen adsorption-desorption isotherms were obtained in a Micromeritics ASAP 2020 instrument. Before analysis, the samples were degassed at 250 °C for 12 h. The specific surface area was determined

using the BET method and pore volume and pore size distribution were determined using the BJH method.

The XRD patterns of the catalysts were obtained using a Panalytical diffractometer equipped with a Pixcel-3D solid-state detector (Empyrean Series 2), using  $\text{CuK}\alpha$  radiation (1.5406 Å), operating at 40 kV and 40 mA. Scans were recorded in the  $10^\circ \leq 2\theta \leq 90^\circ$  interval using a step size of 0.01° and a step time of 6 s. The identification of the crystalline phases was carried out using the ICSD database.

XPS characterization of the catalyst's surface was performed using a SPECS, NAP-XPS, spectrophotometer equipped with a PHOIBOS 150 1D-DLD analyzer, using a monochromatic Al-K $\alpha$  X-ray source (1486.7 eV) operated at 100 W and 13 kV. The pass energy was set to 90 eV for the survey spectra and at 30 eV for high-resolution spectra with steps of 1 eV and 0.1 eV, respectively. The surface charge compensation was controlled with a flood gun operated at 3 eV and 20 mA. The analysis of the spectra was performed using a binding energy (BE) scale calibrated by adjusting the adventitious carbon C-H to 284.0 eV and for quantification, the values of the Relative Sensitivity Factors (RSF), obtained from the Scofield database were: C 1s (1.0), O 1s (2.93), Co 2p (19.16), Ce 3d (51.62), Zr 3d (7.04) and Ti 2p (7.81). The XPS spectra were analyzed using CasaXPS software and all signals were treated using an Off Shirley background and for analysis of the signals, asymmetric functions were considered using a line shape SGL(p)T(k).

Characterization of morphology and structural parameters was performed using High Resolution Transmission Electron Microscopy (HRTEM). The micrographs were obtained using a Tecnai F20 Super Twin TMP instrument operated at 200 kV. For analysis, samples were dispersed in ethanol thorough out sonication for 30 min before being dropped on carbon-coated copper grid.

Temperature programmed reduction analysis was carried out in an AUTOCHEM 2010 Micromeritics equipment. For the analysis, 200 mg of solid was treated at 400 °C under Ar (flow rate of 50 mL  $\text{min}^{-1}$ , heating rate of 5 °C  $\text{min}^{-1}$ ) for 1 h. Then, the powder was cooled to 50 °C and finally heated to 900 °C under  $\text{H}_2$  (diluted in Ar, 10 vol.%) with a flow rate of 50 mL  $\text{min}^{-1}$  and a heating rate of 10 °C  $\text{min}^{-1}$ .

Temperature programmed desorption of ammonia ( $\text{NH}_3$ -TPD) was performed in an AUTOCHEM 2010 Micromeritics instrument. Briefly, 200 mg of the solid was treated at 400 °C for 1 h (heating rate of 10 °C  $\text{min}^{-1}$ ) under He (flow rate of 30 mL  $\text{min}^{-1}$ ). After cooling down to 150 °C,  $\text{NH}_3$  was adsorbed by exposing the powder to a flow of  $\text{NH}_3$  diluted in He (5 vol.%, flow rate of 30 mL  $\text{min}^{-1}$ ) for 2 h. Then, the gas flow was changed to He (flow rate of 30 mL  $\text{min}^{-1}$ ) for 1 h at 150 °C with the aim to eliminate the physisorbed  $\text{NH}_3$ . Finally,  $\text{NH}_3$  was desorbed by heating from 50 °C to 800 °C under a He flow (heating rate of 10 °C  $\text{min}^{-1}$ , flow rate of 30 mL  $\text{min}^{-1}$ ). The signal was followed by TCD and MS detectors.

Raman spectra were obtained with a Raman confocal instrument, Horiba Jobin Yvon (Labram HR model), using excitation laser with a wavelength of 632.81 nm, spectra were recorded from 100 to 2000  $\text{cm}^{-1}$ ; using a D 0.3 filter, a slit of 600  $\mu\text{m}$ , acquisition time of 20 s.

Thermogravimetric analysis (TGA) was performed on a TA Instruments SDT-Q600 equipment. 20 mg of the powder was deposited in an  $\text{Al}_2\text{O}_3$  capsule and heated from room temperature to 900 °C, heating rate of 5 °C  $\text{min}^{-1}$ , under an air rate flow of 100 mL  $\text{min}^{-1}$ .

### 2.4. Catalytic tests

Activity of catalysts in glycerol selective conversion to lactic acid was evaluated in a batch Parr reactor with a capacity of 250 mL. The catalytic reactions were performed at 250 °C, since at this temperature the conversion of glycerol in presence of cobalt oxide catalysts is favored [38]. The reactor was charged with a solution containing 5 wt% glycerol concentration with a NaOH:glycerol molar ratio of 1, and 0.6 g of catalyst. The reactor was sealed, purged with  $\text{N}_2$  and then heated under autogeneous pressure to 250 °C. After reaching the reaction temperature, it was pressurized with 32 bar of  $\text{N}_2$  (the total pressure was 70 bar)

and the stirring was settled to 650 rpm. The reaction was carried out for 8 h with samples being taken out periodically to follow the progress of reaction in terms of conversion and product selectivity. For analysis of the degree of converted glycerol and product yield, 0.35 mL of each sample is quenched with the addition of 1 mL of 0.5 M H<sub>2</sub>SO<sub>4</sub> followed by the addition of 0.05 mL of isopropanol as an internal standard. The resulting solution was passed through a 0.45 μm filter and analyzed by liquid chromatography (HPLC), Agilent 1200 series chromatograph using a refractive index (RI) and equipped with an ICsep ICE-COREGEL-87H3 column. The column temperature was 70 °C and the mobile phase was a solution of H<sub>2</sub>SO<sub>4</sub> 0.005 M with a flow rate of 0.5 mL min<sup>-1</sup>.

The gas phase was analyzed at 8 h of reaction using an Agilent Technologies gas chromatograph instrument, 6890 N model, equipped with TCD and FID detectors. For analysis, a Carboxen 1010 PLOT silica capillary column (30 m x0.53 mm) and an Agilent DB-PETRO column (50 m x0.2 mm) were used. The temperature of the column was kept at 35 °C for 10 min and then it was raised to 230 °C, heating rate of 20 °C min<sup>-1</sup>, followed by an isotherm for 12 min.

Glycerol (GOL) conversion is calculated with Eq. 1:

$$C_{\text{GOL}} (\%) = ((n_{\text{GOL},\text{in}} - n_{\text{GOL},\text{t}})/n_{\text{GOL},\text{in}}) \times 100 \quad (1)$$

where  $n_{\text{GOL},\text{in}}$  is the initial glycerol moles and  $n_{\text{GOL},\text{t}}$  is the amount of glycerol moles after a certain reaction time. Results are presented with a standard deviation of 1.6.

Selectivity to any product is calculated with Eq. 2:

$$S_i (\%) = (n_i/(n_{\text{GOL},\text{in}} - n_{\text{GOL},\text{t}})) \times 100. \quad (2)$$

where  $n_i$  is the moles of the product formed at the reaction time,  $t$ . Results are presented with a standard deviation of 2.3.

Yield of products is calculated with Eq. 3:

$$Y_i (\%) = (C_{\text{GOL}} * S_i)/100. \quad (3)$$

where  $C_{\text{GOL}}$  is the glycerol conversion and  $S_i$  is the selectivity of the product formed at the reaction time,  $t$ . Results are presented with a standard deviation of 1.0.

TOF is calculated with Eq. 4:

$$\text{TOF} (\text{s}^{-1}) = n_{\text{GOL converted}}/(\text{Co at}\% * t) \quad (4)$$

where  $n_{\text{GOL converted}}$  is the converted moles of glycerol at a reaction time of 15 min ( $t$ ) and Co at% is the percentage of cobalt at the surface of catalyst determined by using XPS characterization. At 15 min reaction time, the glycerol conversion varied between 12–15% among the different catalysts.

Carbon balance is calculated with Eq. 5:

$$C_{\text{balance}} (\%) = ((n_{\text{C},\text{t}} + \sum n_{\text{C},\text{i}})/n_{\text{C},\text{in}}) * 100 \quad (5)$$

where  $n_{\text{C},\text{t}}$  is the carbon moles from unreacted glycerol after a certain reaction time,  $n_{\text{C},\text{i}}$  is the carbon moles from the product formed in the reaction time and  $n_{\text{C},\text{in}}$  is the initial carbon moles from initial glycerol.

### 3. Results and discussion

#### 3.1. Characterization of chemical composition

The experimental content of cobalt, determined by atomic emission analysis, is presented in Table 1. The cobalt loading varied between 19.5 and 20 wt%, values that are close to the nominal cobalt indicating that the wet impregnation method, selected for deposition of the cobalt precursor, favors an almost complete deposition on the different supports. Having comparable cobalt loading on the different supports is an essential feature for comparing reactivity among the catalysts based on other physicochemical properties.

#### 3.2. Characterization of structural and morphological properties of supports and supported cobalt oxide catalysts

Structural properties of the supports and supported catalysts were analyzed by XRD (Fig. 1). In the case of supports, characteristic peaks of the CeO<sub>2</sub> fluorite-like structure (ICSD 98-062-1716) were detected (Fig. 1a). On the other hand, the XRD pattern of ZrO<sub>2</sub> exhibits diffraction peaks that are indexed for two different phases (Fig. 1b): the tetragonal phase (ICSD 98-008-5322) and the monoclinic phase (ICSD 98-017-2161). The Rietveld refinement of the XRD patterns indicates that the predominant phase is monoclinic (m-ZrO<sub>2</sub>) with 74 %, and the remaining 26 % corresponds to the tetragonal phase (t-ZrO<sub>2</sub>). Finally, in the case of TiO<sub>2</sub> characteristic diffraction peaks for the anatase phase (ICSD 98-017-2916) were identified in the XRD pattern (Fig. 1c).

After deposition of the cobalt precursor and calcination at 400 °C for 4 h, the diffractograms show the characteristic peaks of the supports in each catalyst (Fig. 1). Additionally, several diffraction peaks are observed indicating the formation of cobalt oxide, Co<sub>3</sub>O<sub>4</sub>, with spinel-like structure (ICSD 98-002-7498). Those characteristic diffraction peaks are observed regardless of the support used. The diffraction peaks for Co<sub>3</sub>O<sub>4</sub> on CeO<sub>2</sub> support are of low intensity and roughly defined moreover, the diffraction peaks of the Co<sub>3</sub>O<sub>4</sub> phase are wider on CeO<sub>2</sub> than on ZrO<sub>2</sub> and TiO<sub>2</sub> (Fig. 1 and Table 1), all these features indicating that poorly crystalline particles might have been formed, while on ZrO<sub>2</sub> and TiO<sub>2</sub> supports they are of high intensity and sharp, suggesting the formation of more crystalline particles. Furthermore, the diffraction peaks for CeO<sub>2</sub> are broaden after the formation of Co<sub>3</sub>O<sub>4</sub> particles (Table 1), suggesting a modification of the structure, these changes might be attributed to a strong interaction of cobalt species with cerium oxide surface.

Morphology and structure of the catalysts were evaluated using HRTEM characterization (Fig. 2), it is observed that the particles are aggregated and is not possible to distinguish the Co<sub>3</sub>O<sub>4</sub> particles from the particles of the different supports. In the three catalysts, the particles have an undefined morphology. When performing the micrograph analysis, the measured interplanar distance values do not correspond exactly to those reported for supports or cobalt oxide phases previously identified by XRD analysis.

In the case of Co<sub>3</sub>O<sub>4</sub>/CeO<sub>2</sub> catalyst, the measured interplanar distances (3.25 Å) do not matched to the Co<sub>3</sub>O<sub>4</sub> spinel phase, identified by

**Table 1**

Composition, textural and structural properties of supports and catalysts, after calcination at 400 °C for 4 h.

Catalyst	Co (wt%)	2θ main peak position			Peak width (FWHM)		S <sub>BET</sub> (m <sup>2</sup> g <sup>-1</sup> )	V <sub>p</sub> (cm <sup>3</sup> g <sup>-1</sup> )
		Support		Co <sub>3</sub> O <sub>4</sub> Peak (113)	support	Co <sub>3</sub> O <sub>4</sub>		
		Peak (hkl)	2θ					
CeO <sub>2</sub>	—	(111)	28.81	—	0.4	—	133	0.14
Co <sub>3</sub> O <sub>4</sub> /CeO <sub>2</sub>	19.8	(111)	28.80	37.10	0.6	0.31	86	0.09
ZrO <sub>2</sub>	—	(11-1)	28.32	—	0.4	—	120	0.09
Co <sub>3</sub> O <sub>4</sub> /ZrO <sub>2</sub>	19.5	(11-1)	28.39	37.14	0.3	0.15	115	0.16
TiO <sub>2</sub>	—	(011)	25.37	—	0.7	—	114	0.14
Co <sub>3</sub> O <sub>4</sub> /TiO <sub>2</sub>	20.0	(011)	25.45	37.03	0.6	0.20	72	0.09

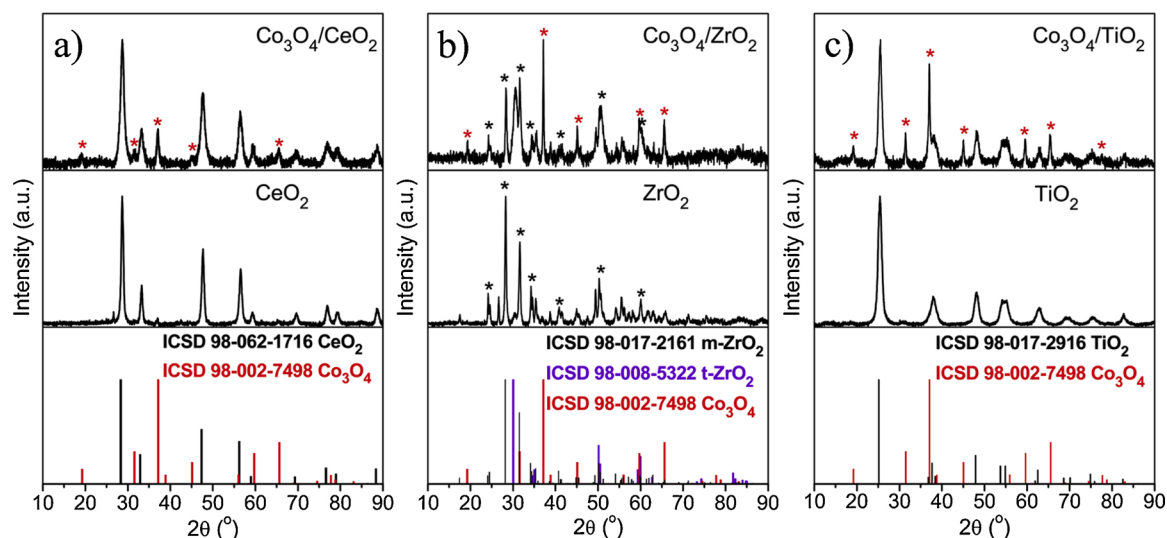


Fig. 1. XRD patterns of a)  $\text{CeO}_2$  and  $\text{Co}_3\text{O}_4/\text{CeO}_2$ , b)  $\text{ZrO}_2$  and  $\text{Co}_3\text{O}_4/\text{ZrO}_2$  and c)  $\text{TiO}_2$  and  $\text{Co}_3\text{O}_4/\text{TiO}_2$ .

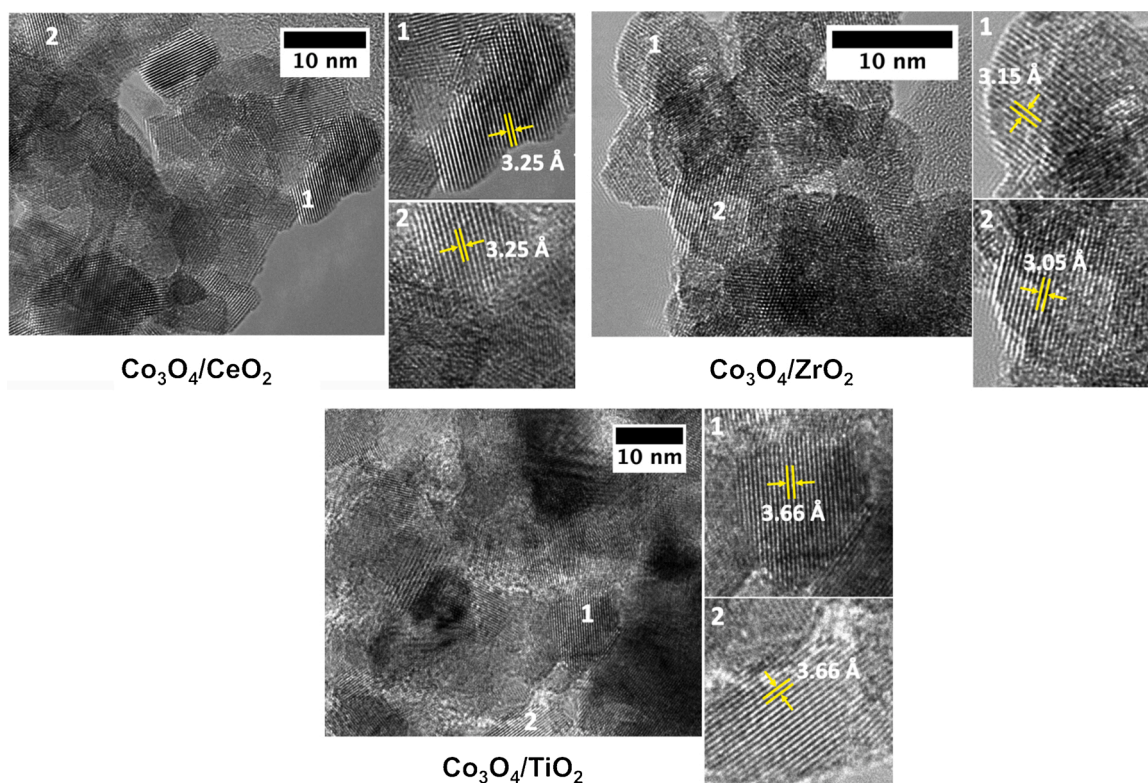


Fig. 2. HRTEM images of catalysts:  $\text{Co}_3\text{O}_4/\text{CeO}_2$ ,  $\text{Co}_3\text{O}_4/\text{ZrO}_2$  and  $\text{Co}_3\text{O}_4/\text{TiO}_2$ .

XRD analysis, but it can be assigned to the  $\text{CeO}_2$  (111) plane, interplanar distance of 3.12 Å. The difference between the distances measured with those reported can be attributed to the presence of the  $\text{Co}_3\text{O}_4$ , as the interaction between both phases modified the structure of  $\text{CeO}_2$  as reported using XRD. It is possible that a strong interaction between the support and the supported phase induced structural changes on  $\text{CeO}_2$  leading to an enlargement of the crystal planes. The radius of  $\text{Ce}^{3+}$  ions is larger than that of  $\text{Ce}^{4+}$  ions,  $\text{Ce}^{3+}$  ions might have been formed on the surface of  $\text{CeO}_2$  because of the formation of oxygen vacancies after  $\text{Co}_3\text{O}_4$  deposition, this phenomenon might originate a lattice expansion or distortion [41,42]. For  $\text{Co}_3\text{O}_4/\text{ZrO}_2$  catalyst, the interplanar distances of  $3.10 \pm 0.05$  Å correspond to the (111) plane of the m- $\text{ZrO}_2$  and (011)

plane of the t- $\text{ZrO}_2$ , the last one far from the reported value of 2.94 Å (ICSD 98-008-5322), which is an indication of changes in the structural parameters of the  $\text{ZrO}_2$  during the cobalt oxide formation. On the other hand, the interplanar distances measured in the  $\text{Co}_3\text{O}_4/\text{TiO}_2$  catalyst, 3.66 Å, do not matched with the interplanar distances of the phases found by XRD, either for  $\text{TiO}_2$  or  $\text{Co}_3\text{O}_4$ . The possible formation of a different structure because of the interaction between cobalt species and the support surface, might be at the origin of the interplanar distances found. It has been reported that the strong interaction between cobalt ions and  $\text{TiO}_2$  can lead to the formation of cobalt titanates [43], with reported interplanar distances of 3.70 Å for plane (012) in  $\text{CoTiO}_3$  phase (ICSD 98-003-8158).

### 3.3. Characterization of textural properties of supports and supported cobalt oxide catalysts

The  $N_2$  adsorption branches of the isotherms for all supports show that they correspond to type IV (Fig. 3), indicating the presence of pores with diameters in the mesopore range (Fig. 3 inset, Table 1), although the isotherm of  $ZrO_2$  does not show a clear capillary condensation step [44]. The  $N_2$  desorption branches of the isotherms show differences in their shape, wherein  $CeO_2$  exhibits a hysteresis of H1 type (Fig. 3), which indicates the presence of cylindrical pores,  $ZrO_2$  and  $TiO_2$  exhibit both H2 type hysteresis (Fig. 3), evidencing i) the presence of pores without a defined shape or ii) the occurrence of different condensation/evaporation mechanisms in pores with narrow openings and pores with large diameter size [44]. After deposition and calcination of the cobalt precursor, the shape of the isotherms remains unchanged (Fig. 3), however the adsorbed volume of  $N_2$  decreased for  $Co_3O_4/CeO_2$  and  $Co_3O_4/TiO_2$ , which might be due to the formation of  $Co_3O_4$  particles blocking in some extent the access to the support surface and porosity. Meanwhile, the isotherm of the  $Co_3O_4/ZrO_2$  powder is similar to that of the bare support,  $ZrO_2$ , showing a slightly increase in the amount of adsorbed  $N_2$  with respect to the bare support at high  $P/P_0$  values (Fig. 3), indicating that during deposition and calcination of the cobalt precursor no significant changes occurred in the textural properties of the support.

### 3.4. Characterization of chemical surface properties of supported cobalt oxide catalysts

Surface composition of  $Co_3O_4$  supported catalysts is performed by XPS (Fig. 4) and results are gathered in Table S1. The analysis indicated that although the cobalt loading in all catalysts is comparable, 19.5–20 wt%, the cobalt concentration at the surface is lower on  $CeO_2$  than on  $ZrO_2$ , reaching 2.3 and 4.2 at% respectively, both being significantly lower than on  $TiO_2$ , 7.7 at% (Table S1). The analysis of the high-resolution spectrum of Co2p core level in all three catalysts is showing similar features in the photopeak profile, with its characteristic doublet  $Co2p_{3/2}$  and  $Co2p_{1/2}$  due to the spin-orbit coupling, each

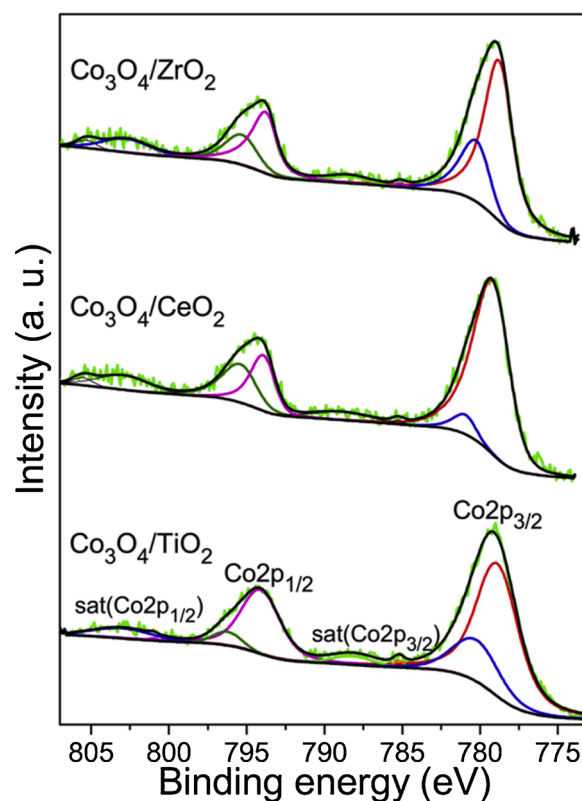


Fig. 4. High-resolution XPS spectra for Co2p core level:  $Co_3O_4/ZrO_2$ ,  $Co_3O_4/CeO_2$ ,  $Co_3O_4/TiO_2$ .

photopeak showing the corresponding shake-up satellite structure at higher binding energy (Fig. 4), these results indicating the presence of both  $Co^{2+}$  and  $Co^{3+}$  in  $Co_3O_4$  [45,46]. The best fitting of the spectra showing 8 signals (Fig. 4). The  $Co2p_{3/2}$  and  $Co2p_{1/2}$  photopeaks are both

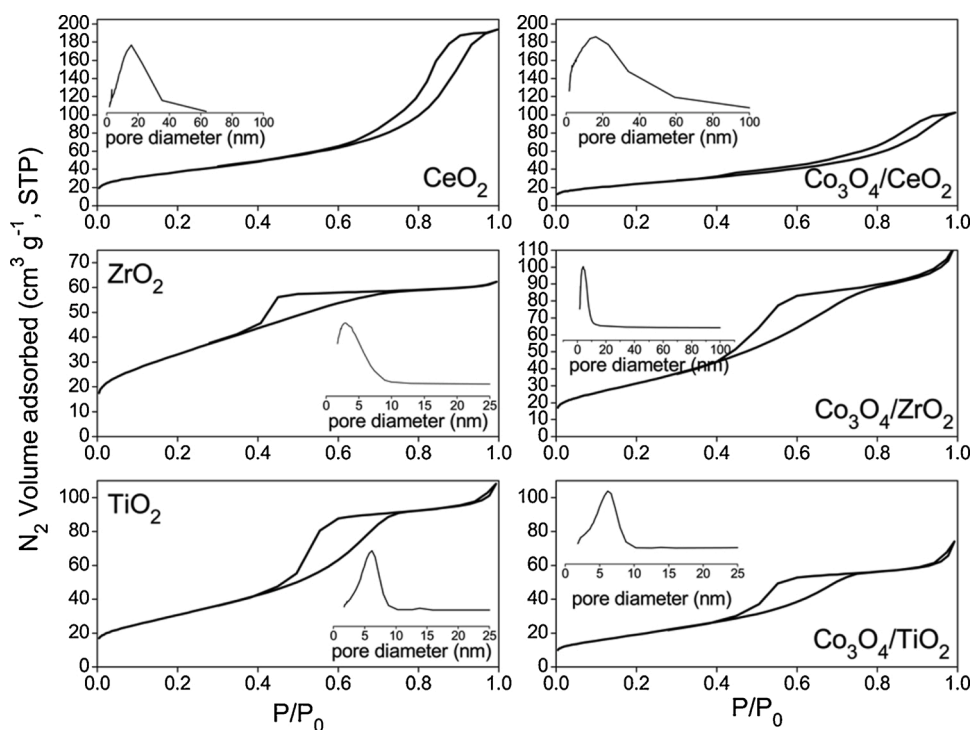


Fig. 3.  $N_2$  adsorption-desorption isotherms and pore size diameter distribution for i)  $CeO_2$ ,  $ZrO_2$ ,  $TiO_2$  supports and ii)  $Co_3O_4/CeO_2$ ,  $Co_3O_4/ZrO_2$ ,  $Co_3O_4/TiO_2$  powders.

convoluted in 2 peaks (Fig. 4), the peaks centered at  $778.8 \pm 0.1$  and  $793.8 \pm 0.3$  eV are assigned to  $\text{Co}^{3+}$  species while the peaks centered at  $780.3 \pm 0.3$  and  $795.6 \pm 0.5$  eV are assigned to  $\text{Co}^{2+}$  species in  $\text{Co}_3\text{O}_4$  [46].

$\text{Co}_3\text{O}_4$  crystal possesses 56 atoms in the unit cell with face-centered-cubic lattice structure formed by packed  $\text{O}^{2-}$  ions, 16 octahedral sites occupied by  $\text{Co}^{3+}$  ions and 8 tetrahedral sites occupied by  $\text{Co}^{2+}$  ions [45]. According to fitting of the XPS spectra (Fig. 4 and Table S1), the main contribution to the  $\text{Co}2\text{p}_{3/2}$  signal arose from  $\text{Co}^{3+}$  ions, the area ratio  $\text{Co}^{2+}/\text{Co}^{3+}$  reached 0.33 in  $\text{Co}_3\text{O}_4/\text{ZrO}_2$ , 0.32 in  $\text{Co}_3\text{O}_4/\text{TiO}_2$ , and 0.07 in  $\text{Co}_3\text{O}_4/\text{CeO}_2$ . These results indicating that non-stoichiometric  $\text{Co}_3\text{O}_4$  particles might have been formed on the surface of the different supports, the low  $\text{Co}^{2+}/\text{Co}^{3+}$  reached in  $\text{Co}_3\text{O}_4/\text{CeO}_2$  catalyst suggesting that  $\text{Co}^{3+}$  ions have been stabilized on the surface of  $\text{CeO}_2$  which, in agreement with XRD characterization, is indicating that low crystalline crystallites have been formed.

### 3.5. Reduction of supports and supported cobalt oxide catalysts

To determine the number and type of reducible species in the catalysts,  $\text{H}_2$ -TPR analysis was performed (Fig. 5 and Table S2). As a first remark, the TPR profiles of supports show reduction peaks roughly defined and of low intensity, indicating a low hydrogen consumption: for analysis, they were normalized in an attempt to provide a clearer analysis of the signals. On the contrary, high-intensity reduction events are observed on the TPR profiles of  $\text{Co}_3\text{O}_4$  containing catalysts. It is reported that  $\text{Co}_3\text{O}_4$  follows a two-step reduction, the first one attributed to the reduction of  $\text{Co}^{3+}$  to  $\text{Co}^{2+}$  and the second one, attributed to the reduction of  $\text{Co}^{2+}$  to  $\text{Co}^0$  [47,48].

The TPR profile of  $\text{CeO}_2$  shows two main reduction events at  $442^\circ\text{C}$  and  $711^\circ\text{C}$  (Fig. 5), indicating the reduction of surface and bulk oxygen species respectively, while the shoulder at  $\sim 300^\circ\text{C}$  is assigned to the reduction of non-stoichiometric  $\text{CeO}_x$  oxides [35,49–51]. The TPR profile of  $\text{Co}_3\text{O}_4/\text{CeO}_2$  exhibits two main reduction events at lower temperatures. The first reduction step of  $\text{Co}_3\text{O}_4/\text{CeO}_2$  centered at  $247^\circ\text{C}$  corresponds to the reduction of  $\text{Co}^{3+}$  to  $\text{Co}^{2+}$  and the second one,

centered at a temperature of  $310^\circ\text{C}$  to the reduction of  $\text{Co}^{2+}$  to  $\text{Co}^0$ . The shoulder in the second peak ( $\sim 400^\circ\text{C}$ ) suggests *i)* the reduction of non-stoichiometric  $\text{CeO}_x$  oxides as observed in the bare support or *ii)* that after the first reduction event, two species of  $\text{Co}^{2+}$  are generated, where the one that is interacting to a greater degree with the support is more easily reducible given the storage capacity of oxygen in the  $\text{CeO}_2$  support [52]. For  $\text{ZrO}_2$ , the TPR profile shows four reduction events at temperatures higher than  $350^\circ\text{C}$  (Fig. 5). Two main reduction peaks centered at  $474^\circ\text{C}$  and  $606^\circ\text{C}$ , might be correlated to the reduction of carbonates and surface hydroxyl groups [53,54]. For  $\text{Co}_3\text{O}_4/\text{ZrO}_2$ , four reduction peaks are observed at lower temperatures than for  $\text{ZrO}_2$  support, indicating the formation of four reducible species of cobalt oxide. The presence of several signals associated with the reduction of  $\text{Co}_3\text{O}_4$  might be due to *i)* the presence of different reducible cobalt species, either  $\text{Co}^{2+}$  or  $\text{Co}^{3+}$ , with different degrees of interaction with the support surface, indicating that the catalyst presents a high heterogeneity in its speciation and *ii)* the formation of particles with different size, since this parameter is decisive in the reduction processes of cobalt oxides [55]. In the case of  $\text{TiO}_2$ , it is reduced in a wide temperature range with a main peak centered at  $496^\circ\text{C}$ , in general it is reported that no evident reduction peaks are observed for  $\text{TiO}_2$  [56,57]. In the TPR profile of  $\text{Co}_3\text{O}_4/\text{TiO}_2$  (Fig. 5), four reduction peaks are observed, where the reduction peaks at  $274^\circ\text{C}$  and  $360^\circ\text{C}$  might be attributed to the two-step reduction of  $\text{Co}_3\text{O}_4$ , the reduction at higher temperatures,  $360^\circ\text{C}$  and  $394^\circ\text{C}$ , might be attributed to *i)* the presence of different reducible  $\text{Co}^{n+}$  species in different degrees of interaction with the support surface or formation of particles with different size and *ii)* the presence of  $\text{Co}^{2+}$  species in strong interaction with  $\text{TiO}_2$  surface, possibly forming titanate-like species [58]. If these species are formed during catalyst preparation, they were not identified using XRD because of their amorphous nature or these species were highly dispersed with crystallite sizes of less than  $\sim 4$  nm, although lattice fringes suggesting the formation of  $\text{CoTiO}_3$  phase were identified using HRTEM.

The results of  $\text{H}_2$ -TPR characterization evidenced a strong dependence of cobalt species formed and their reducibility on the support nature, thus the support chemical composition influenced the

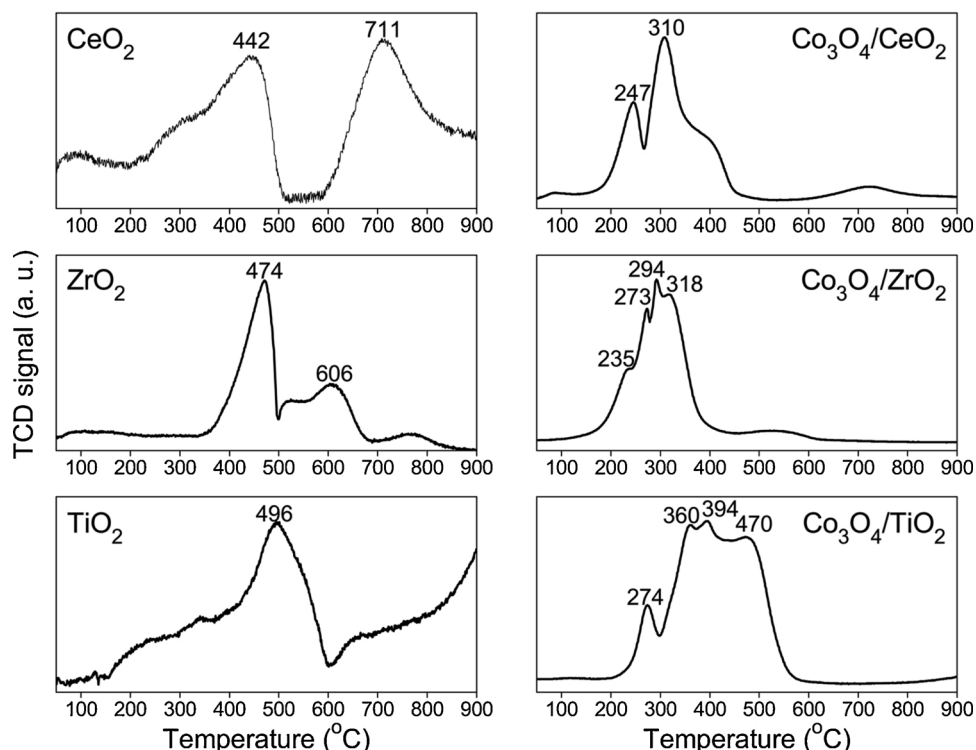


Fig. 5. TPR profiles for supports:  $\text{CeO}_2$ ,  $\text{ZrO}_2$ ,  $\text{TiO}_2$ , and catalysts:  $\text{Co}_3\text{O}_4/\text{CeO}_2$ ,  $\text{Co}_3\text{O}_4/\text{ZrO}_2$ ,  $\text{Co}_3\text{O}_4/\text{TiO}_2$ .

composition of the catalyst, particularly the homogeneity of cobalt reducible species formed. Mainly two types of reducible species in  $\text{Co}_3\text{O}_4/\text{CeO}_2$  were formed while in  $\text{Co}_3\text{O}_4/\text{ZrO}_2$  and  $\text{Co}_3\text{O}_4/\text{TiO}_2$  four reduction events are observed. Additionally, the support influences the temperature at which the cobalt species reduction occurs, lower reduction temperatures being observed when  $\text{CeO}_2$  or  $\text{ZrO}_2$  are used as support, probably because on the surface these supports generate a reducing environment for the supported particles.  $\text{CeO}_2$  exhibits redox properties and has a high oxygen storage capacity [41,52], which allows the reduction of the  $\text{Co}_3\text{O}_4$  particles to occur at a lower temperature compared to unsupported  $\text{Co}_3\text{O}_4$  nanoparticles. The changes observed in the XRD pattern and HRTEM for  $\text{CeO}_2$  after formation of  $\text{Co}_3\text{O}_4$  suggested a modification of the structure, these changes might be attributed to a strong interaction of cobalt species with cerium oxide surface and perhaps is also responsible for the stabilization of  $\text{Co}^{n+}$  species being reduced at low temperature. The formation of an oxygen vacancy on  $\text{CeO}_2$  lattice generates 2 electrons which remain on the surface [41], leading to a reducing environment favoring interaction with  $\text{Co}^{n+}$  species. In the case of the  $\text{ZrO}_2$  support, the presence of  $\text{Zr}^{3+}$  species on the surface has been reported to generate anion vacancies, thus creating a reducing environment [59], while the strong metal-support interaction on  $\text{TiO}_2$  generates the stabilization of oxidized cobalt species, which are reduced at high temperatures.

### 3.6. Characterization of the acid properties of supports and supported cobalt oxide catalysts

The acidity properties in terms of number of sites, strength and density of acid sites for supports and supported cobalt oxide catalysts were analyzed by  $\text{NH}_3$ -TPD (Fig. 6 and Table S2). The strength of the acid sites is classified in accordance to the desorption temperature of  $\text{NH}_3$ : i) weak strength corresponds to  $\text{NH}_3$  desorbed at temperatures below  $200^\circ\text{C}$ , ii) medium strength for  $\text{NH}_3$  desorbed in the  $200$ – $400^\circ\text{C}$  temperature range, and iii) strong acid sites for  $\text{NH}_3$  desorbed at temperatures higher than  $400^\circ\text{C}$ .

$\text{ZrO}_2$  and  $\text{TiO}_2$  acid site densities are more than 2 times higher than

for  $\text{CeO}_2$  (Table S2).  $\text{CeO}_2$  exhibits three different types of acid sites (Fig. 6), with medium strength and strong acid sites, while  $\text{ZrO}_2$  exhibits the highest density of acidic sites with weak, medium and strong strength. In both,  $\text{CeO}_2$  and  $\text{ZrO}_2$ , the main contribution to the acidity arose from acidic sites with strong acidity while in the case of  $\text{TiO}_2$ , the main contribution to the acidity is found from sites with medium strength (Fig. 6 and Table S2). The presence of acid sites on  $\text{ZrO}_2$  is attributed to  $\text{Zr}^{n+}$  ions which behave as Lewis acids [60]. Nevertheless, the m- $\text{ZrO}_2$  phase exhibits a combination of Brønsted and Lewis acid sites, while the t- $\text{ZrO}_2$  phase only exhibits Lewis acid sites [61]. The presence of  $\text{Zr}^{4+}$  ions with different coordination in  $\text{ZrO}_2$  phases might be at the origin of acidic sites with different strength [62],  $\text{ZrO}_2$  shows four different acidic sites reflecting the heterogeneity in the type/strength of acid sites (Fig. 6). In the case of  $\text{TiO}_2$ , the anatase phase exhibits Lewis acid sites [63,64].

After formation of  $\text{Co}_3\text{O}_4$  on the different supports, the total density of acid sites increases in all cobalt oxide containing powders (Table S2). On  $\text{Co}_3\text{O}_4/\text{CeO}_2$  catalyst only a slightly variation on the density of acid sites with medium strength is observed (Fig. 6), perhaps because  $\text{Co}_3\text{O}_4$  also exhibits acid sites with different strength [65]. For  $\text{Co}_3\text{O}_4/\text{ZrO}_2$  and  $\text{Co}_3\text{O}_4/\text{TiO}_2$  catalysts, there is a significant increase in the acid sites density, which is mainly reflected in the increase of strong acid sites (Fig. 6). This indicates that the presence of cobalt oxide in interaction with the surface of  $\text{ZrO}_2$  and  $\text{TiO}_2$  modifies the acidic properties of these supports.

### 3.7. Evaluation of catalytic properties on glycerol conversion to lactic acid

Reaction is initially performed without heterogeneous catalysts *i.e.* hydrothermal conditions, in order to evidence the effect of temperature, pressure and NaOH on the conversion process of glycerol (GOL) (Fig. S1). At  $250^\circ\text{C}$ , GOL conversion continuously increased from 12 % at the beginning of the reaction until reaching 48 % after 8 h reaction. In the liquid phase identified products were lactic acid (LA), pyruvaldehyde (PYR), glyceraldehyde (GLY), 1,2-propanediol (1,2-PDO), hydroxyacetone (HA) and acetic acid (AA), while in the gas phase

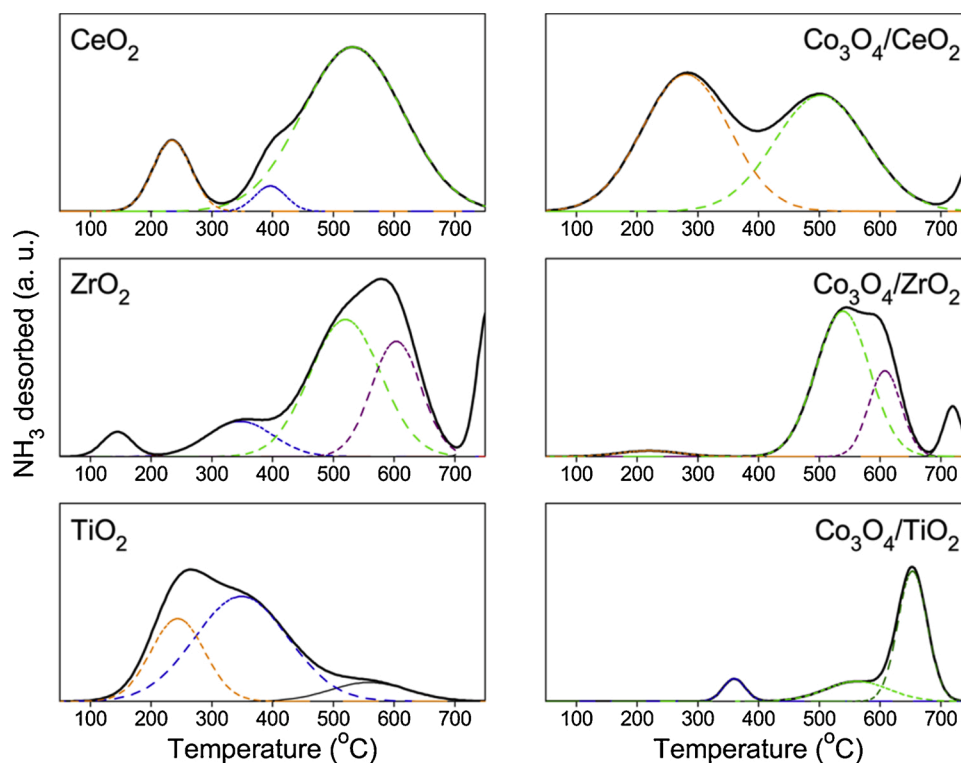


Fig. 6.  $\text{NH}_3$ -TPD profiles for supports:  $\text{CeO}_2$ ,  $\text{ZrO}_2$ ,  $\text{TiO}_2$ , and catalysts:  $\text{Co}_3\text{O}_4/\text{CeO}_2$ ,  $\text{Co}_3\text{O}_4/\text{ZrO}_2$ ,  $\text{Co}_3\text{O}_4/\text{TiO}_2$ .

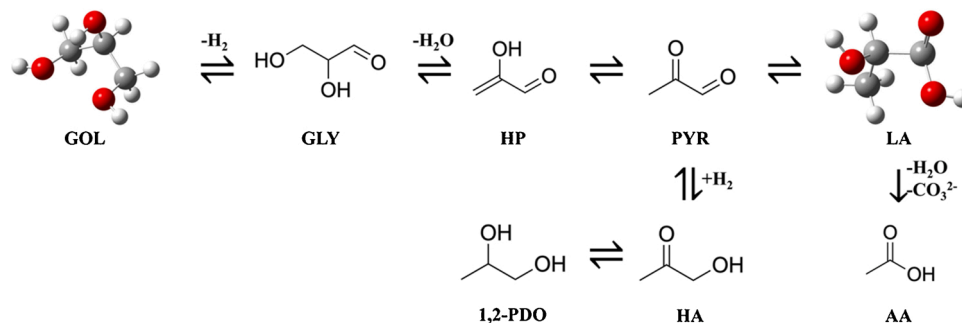
hydrogen ( $H_2$ ) was the formed product. During reaction, the main products formed are LA and PYR, LA reaching a maximum yield of 32.9 % at 8 h reaction. Other products formed such as GLY, HA, 1,2-PDO and AA are not exceeding 1.6 % yield during the reaction. According to different reported studies on GOL conversion to LA [33,66–69], the reaction route included the dehydrogenation of GOL to produce GLY (Scheme 1), GLY forming an equilibrium with dihydroxyacetone (DHA) [69], but DHA was not identified under the current reaction conditions. The formed GLY then produced PYR *via* and oxidative dehydration through 2-hydroxypropenal intermediate (HP), the later leading to a 2-hydroacetone keto-enol tautomerism allowing the formation of PYR, finally LA can be obtained from PYR *via* an intramolecular benzyl acid or Cannizzaro type rearrangement [66,68]. The formation of low amounts of HA and 1,2-PDO can be attributed to the hydrogenation of PYR with  $H_2$  formed in the process of the dehydrogenation of GOL, while the formation of acetic acid (AA) has been reported as a LA decomposition reaction in a basic medium at high temperatures [67].

Results of glycerol conversion, lactic acid and piruvaldehyde yields, and carbon balance in presence of the different catalysts are presented in Fig. 7 and gathered in Table 2 and Table S3. As a first remark, the identified products in liquid (Scheme 1) and gas phases are the same as in the case of the reaction without heterogeneous catalysts, indicating that the reaction route to obtain LA from GOL is not modified by the presence of the different catalysts. Performing the reaction in presence of the bare supports,  $CeO_2$  or  $TiO_2$ , no significant differences in terms of GOL conversion and LA yield are observed with regard to the hydrothermal reaction, indicating that these two supports have no significant activity in the reaction. On the other hand,  $ZrO_2$  favors the GOL conversion, reaching a maximum of 77 % after 8 h reaction (Fig. 7). This might be attributed to the acidic properties of the  $ZrO_2$  polymorph, the m- $ZrO_2$  phase possesses surface OH groups, either terminal or multi-coordinated [70], which might favor on the surface the dehydrogenation of the adsorbed primary alcohol [71] besides, the high density of acidic sites on  $ZrO_2$  might favor activation of the intermediate aldehydes. Consequently, LA yield increased reaching 51 % when using  $ZrO_2$  as catalyst. Nevertheless, carbon balance decreased with reaction time after 2 h indicating that side reactions or carbon deposition is occurring, despite a continuous increase in GOL conversion with reaction time, LA yield did not significantly increase after 2 h reaction, thus the high density of acid sites and with strong acidity might led to LA decomposition leading to coke formation.

Conversion of GOL increased when using  $Co_3O_4/CeO_2$  and  $Co_3O_4/ZrO_2$  catalysts with respect to the bare supports, following a pseudo-first order kinetic order (Fig. 7), indicating that  $Co_3O_4$  favored adsorption and activation of GOL, perhaps  $Co_3O_4$  mediated in the initial dehydrogenation step of the adsorbed primary GOL to produce GLY. However, on  $Co_3O_4/TiO_2$  catalyst conversion of GOL remained similar to the  $TiO_2$  catalyst and hydrothermal conditions, showing that neither  $TiO_2$  nor  $Co_3O_4/TiO_2$  have activity for converting GOL. These results suggest that the support type influenced activity of  $Co_3O_4$  active phase on GOL selective partial oxidation to LA. TOF was calculated following the order:

$Co_3O_4/CeO_2 (1.2 \times 10^{-1} s^{-1}) > Co_3O_4/ZrO_2 (8.3 \times 10^{-2} s^{-1}) > Co_3O_4/TiO_2 (3.0 \times 10^{-2} s^{-1})$ . These results indicate that  $Co_3O_4/CeO_2$  is the most active catalyst in converting glycerol to lactic acid. Conversion is greater with  $Co_3O_4/ZrO_2$  catalyst, reaching up to 93 % at 8 h, while with  $Co_3O_4/CeO_2$  reaches 78 % (Fig. 7 and Table S3). The higher conversion reached with  $Co_3O_4/ZrO_2$  might be attributed to the support acidic properties [72,73], which might favor adsorption and activation of primary OH groups of GOL or the activation of the intermediate aldehydes. LA is the main product formed with both,  $Co_3O_4/CeO_2$  and  $Co_3O_4/ZrO_2$  catalysts during the whole reaction time, the increasing in GOL conversion with reaction time being in favor of LA yield, reaching 67 % after 8 h reaction with both catalysts while on  $Co_3O_4/TiO_2$ , only reached 33 %. These results evidenced that  $TiO_2$  is not a suitable support for  $Co_3O_4$  active phase in GOL selective conversion to LA. In the case of  $Co_3O_4/TiO_2$ , the formation of cobalt titanates, as proposed with the results of characterization by  $H_2$ -TPR and HR-TEM, might hinder activity of cobalt species perhaps because of a strong interaction between cobalt and titania led to less active cobalt species on the catalyst' surface. Furthermore, during reaction the  $Co^{3+}$  ions are reduced (see characterization of the spent catalyst below) while GOL is oxidized, and the presence of water might, to some extent, favor the formation of cobalt titanates [74].

LA is the main formed product under hydrothermal conditions, in presence of the bare supports or using cobalt oxide-based catalysts (Fig. 7). The increase in conversion of GOL with reaction time being in favor of LA yield. At comparable GOL conversion in the range  $53.5 \pm 5.5$  %, LA selectivity is higher using  $Co_3O_4/CeO_2$  catalyst (Table 2). At 8 h reaction time when the highest conversions of GOL are obtained, the highest selectivity to LA is obtained using  $CeO_2$  support for  $Co_3O_4$  (Table S3). Although  $Co_3O_4/ZrO_2$  led to the highest GOL conversion among the different catalysts, the selectivity toward LA is lower than using  $Co_3O_4/CeO_2$ , reaching 72.8 and 85.6 %, respectively (Table S3). Studies reported in literature on GOL valorization using heterogeneous catalysts with different acid-base properties, evidenced that their activity strongly depended on the total acidity of catalysts, especially because it influenced the dehydration reactions [72]. Supports with acid properties led to the generation of C3 products, GLY yield was mostly favored on catalysts with a low number of acidic sites [72,73]. The results of  $NH_3$ -TPD showed that  $Co_3O_4/ZrO_2$  exhibited a wide distribution of acid sites with different strengths, with main contribution to the total acidity arising from the strong acid sites, while  $Co_3O_4/CeO_2$  exhibited a more balanced acidity between medium-strong strength acid sites. The total acidity of  $Co_3O_4/ZrO_2$  being largely higher than that of  $Co_3O_4/CeO_2$ . For instance, although high acidity favored a higher conversion of GOL on  $Co_3O_4/ZrO_2$ , it causes a significant decrease in LA selectivity (Tables 2 and S3). After 2 h reaction time, carbon balance decreased when using  $Co_3O_4/ZrO_2$  catalyst while it remained almost constant when using  $Co_3O_4/CeO_2$  catalyst (Fig. 7). According to the literature on PYR activation to produce LA on m- $ZrO_2$  catalysts [62], carbonyl groups are adsorbed and activated on coordinatively unsaturated  $Zr^{4+}$  ions, although this can favor selectivity to LA it also suggests that high acidity led to the formation of carbonaceous species adsorbed on the catalyst or



Scheme 1. Reaction pathway according to identified products.

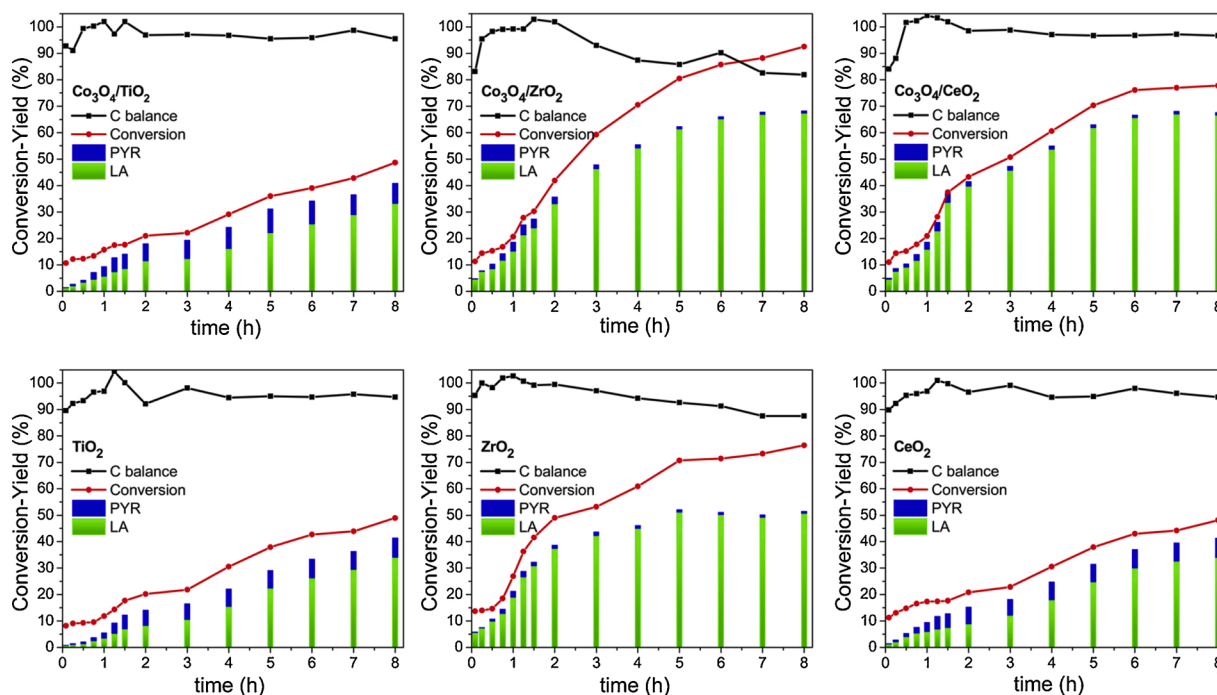


Fig. 7. Evolution of glycerol conversion, product yield and carbon balance with bare supports and  $\text{Co}_3\text{O}_4/\text{CeO}_2$ ,  $\text{Co}_3\text{O}_4/\text{ZrO}_2$ ,  $\text{Co}_3\text{O}_4/\text{TiO}_2$  catalysts.

Table 2

Selectivity and Yield to LA at comparable GOL conversion ( $53.5 \pm 5.5$  %).

Catalyst	$C_{\text{GOL}}$ (%)	$S_{\text{LA}}$ (%)	$Y_{\text{LA}}$ (%)
hydrothermal	48	69	33
$\text{CeO}_2$	48	71	34
$\text{ZrO}_2$	49	76	37
$\text{TiO}_2$	49	70	34
$\text{Co}_3\text{O}_4/\text{CeO}_2$	51	90	46
$\text{Co}_3\text{O}_4/\text{ZrO}_2$	59	78	46
$\text{Co}_3\text{O}_4/\text{TiO}_2$	49	68	33

coke formation, as LA selectivity was lower on  $\text{Co}_3\text{O}_4/\text{ZrO}_2$  catalyst but also carbon balance only reached  $\sim 82$  %, while on  $\text{Co}_3\text{O}_4/\text{CeO}_2$  reached  $\sim 97$  % (Fig. 7 and Table S3). Low carbon balance is also evidenced with  $\text{ZrO}_2$  alone as catalyst, the high density of strong acid sites can lead to strongly adsorbed PYR, generating the formation of carbonaceous deposits, as it has been reported in catalysts with high acidity [75]. Characterization of the recovered catalysts after the reaction using TGA analysis shows a weight loss of  $\sim 15$  % for  $\text{Co}_3\text{O}_4/\text{ZrO}_2$  catalyst in the temperature range of 200–700 °C (Fig. S2), indicating that strongly adsorbed carbonaceous species remain on the catalyst surface while the weight loss for  $\text{Co}_3\text{O}_4/\text{CeO}_2$  catalyst is lower than 5 % in the temperature range of 200–450 °C.

Either on  $\text{Co}_3\text{O}_4/\text{ZrO}_2$  or  $\text{Co}_3\text{O}_4/\text{CeO}_2$  catalysts, conversion of GOL, selectivity and yield to LA were higher than on  $\text{ZrO}_2$  or  $\text{CeO}_2$ , indicating that  $\text{Co}_3\text{O}_4$  plays a key role for activating GOL and selectively forming LA. For instance,  $\text{Co}_3\text{O}_4/\text{CeO}_2$  catalyst with less exposed cobalt on the surface, with medium strength acid sites and more homogenous composition in terms of reducible species of cobalt species at low temperatures, is at the origin of the better performance of GOL selective conversion to LA. As observed using XPS characterization,  $\text{Co}_3\text{O}_4/\text{CeO}_2$  catalyst is enriched in  $\text{Co}^{3+}$  species at the surface, in  $\text{H}_2$ -TPR results  $\text{Co}^{3+}$  species in  $\text{Co}_3\text{O}_4$  supported on  $\text{CeO}_2$  are reduced at a temperature close to the reaction temperature, thus although TPR is performed under  $\text{H}_2$ , alcohols are reducing agents and it might be inferred that while GOL is adsorbed and oxidized to GLY,  $\text{Co}^{3+}$  species must be reduced. The presence of acid sites with middle strength might allow the activation of

the intermediate aldehydes leading to the formation of LA avoiding side reactions and coke formation.

In recent years, several reports in literature have evidenced the potential of transition metals-based heterogeneous catalysts for selectively converting GOL to LA, the results of some of these reports are summarized in Table S4. In comparison, the results reported in this work with  $\text{Co}_3\text{O}_4/\text{CeO}_2$  catalyst are in line with the obtained with copper-based catalysts,  $\text{Co}_3\text{O}_4/\text{CeO}_2$  catalyst allowed high conversion of GOL with high selectivity to LA at stoichiometric mole ratio between GOL and NaOH, and moderate  $\text{N}_2$  pressure.

### 3.8. Characterization of catalysts after reaction and cyclability

The solids recovered after 8 h reaction were washed, dried and further calcined for 4 h at 400 °C (regeneration process) and then characterized to determine the compositional, structural, and morphological changes induced during reaction. Regardless of the support type, the cobalt content decreased indicating leaching of the supported phase during the reaction (Table S5). The extend of cobalt leaching is less important with  $\text{TiO}_2$  support, which might be attributed to the formation of cobalt titanate species, where cobalt species are in strong interaction with the support surface.

Catalysts recovered after reaction are denoted as  $\text{Co}_3\text{O}_4/\text{support R}$ , where support is:  $\text{CeO}_2$ ,  $\text{ZrO}_2$ ,  $\text{TiO}_2$ , and R indicates recovered after reaction without calcination. In this way, catalysts recovered and calcined are denoted with the same abbreviation,  $\text{Co}_3\text{O}_4/\text{support}$ , changing R for C. Characterization by XRD shows that for  $\text{Co}_3\text{O}_4/\text{CeO}_2$  R catalyst, the fluorite-like structure of the support is identified but diffraction peaks for  $\text{Co}_3\text{O}_4$  phase are not observed, instead identified phases are metallic Co and CoO (Fig. 8), these observations indicate that the support does not undergo structural changes during the reaction, but the  $\text{Co}^{3+}$  and  $\text{Co}^{2+}$  ions present in the  $\text{Co}_3\text{O}_4$  spinel are reduced to  $\text{Co}^0$  and  $\text{Co}^{2+}$ . Alcohols are reducing agents and as glycerol is adsorbed and oxidized on the surface of the catalyst, the surface  $\text{Co}^{n+}$  ions are reduced indicating that cobalt oxide is an active species during reaction. Raman spectra (Fig. S3) recorded on the spent catalysts without calcination are also indicating major changes in the catalysts, the peaks for  $\text{Co}_3\text{O}_4$  phase are not observed after reaction. After calcination ( $\text{Co}_3\text{O}_4/\text{CeO}_2$  C), the XRD

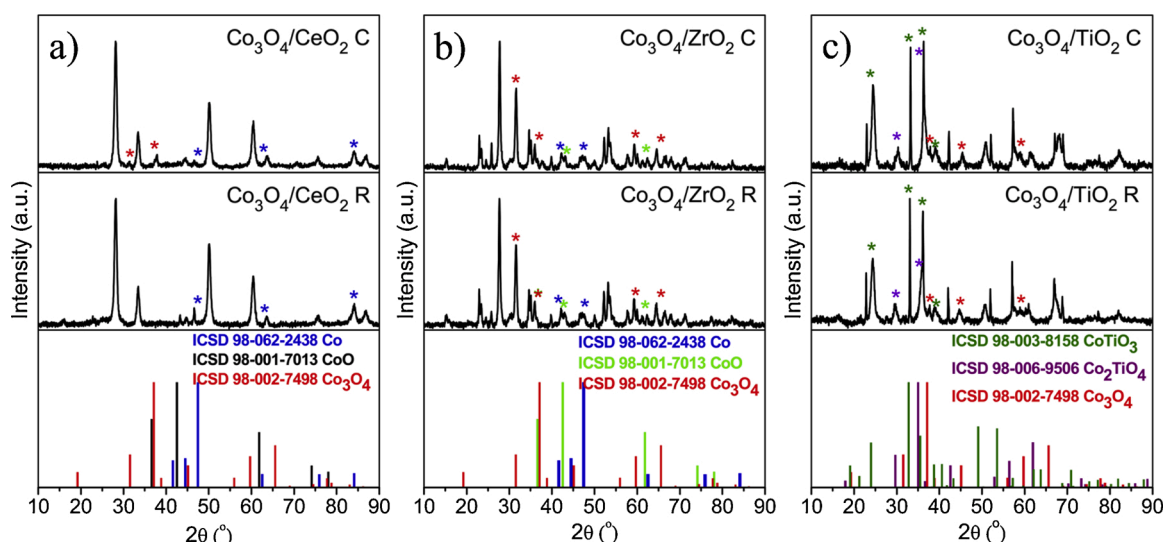


Fig. 8. XRD patterns of the catalysts recovered (R) and calcined (C) after reaction a)  $\text{Co}_3\text{O}_4/\text{CeO}_2$ , b)  $\text{Co}_3\text{O}_4/\text{ZrO}_2$ , c)  $\text{Co}_3\text{O}_4/\text{TiO}_2$ .

pattern indicates the regeneration of the  $\text{Co}_3\text{O}_4$  phase, but the CoO phase remains in the catalyst suggesting that a fraction of the cobalt is not completely oxidized at the calcination conditions. In the case of  $\text{Co}_3\text{O}_4/\text{ZrO}_2$  R, the diffraction pattern indicates that  $\text{Co}_3\text{O}_4$  is reduced to metallic Co (Fig. 8), Raman spectra for the catalyst recorded after reaction did not show signals for  $\text{Co}_3\text{O}_4$  phase (Fig. S3). Additionally, diffraction peaks associated with a carbonaceous species are also identified at  $2\theta$  of  $\sim 26.6^\circ$ , corroborating that the high density of strong acid sites leads to coke formation. After calcination, the XRD pattern of  $\text{Co}_3\text{O}_4/\text{ZrO}_2$  C shows that cobalt is forming  $\text{Co}_3\text{O}_4$  spinel-like structure and metallic Co (Fig. 8), in addition the carbonaceous species are still identified indicating that calcination at  $400^\circ\text{C}$  is not enough to remove such carbonaceous deposits on the surface of the catalyst. Additional characterization of the catalysts by Raman spectroscopy (Fig. S3), displayed further evidence of coke formation due to the presence of the characteristic bands of carbonaceous materials, bands D and G at  $1336$  and  $1586\text{ cm}^{-1}$  respectively, before and after calcination. TGA analysis showed that a calcination at  $700^\circ\text{C}$  is necessary to eliminate the carbonaceous species formed or adsorbed during reaction (Fig. S2). Nevertheless, initially during preparation of catalysts, they were calcined at  $400^\circ\text{C}$ , thus high reaction temperatures could favor sintering of the particles which will make the catalysts not comparable before and after reaction. Finally, the XRD pattern of  $\text{Co}_3\text{O}_4/\text{TiO}_2$  R shows the formation of mixed structures between cobalt and titanium (Fig. 8), identified phase is  $\text{Co}_2\text{TiO}_4$  (ICSD 98-006-9506). It is possible that during reaction, the reduction of  $\text{Co}_3\text{O}_4$  at high reaction temperature, the strong metal-support interaction directed the formation of cobalt titanates such as  $\text{CoTiO}_3$  and/or  $\text{Co}_2\text{TiO}_4$ , according to the catalytic results these species do not have catalytic activity in the reaction and avoid cobalt species to convert glycerol into lactic acid. After calcination, the XRD pattern of  $\text{Co}_3\text{O}_4/\text{TiO}_2$  C exhibits characteristic peaks for titanate species and no characteristic diffraction peaks for  $\text{Co}_3\text{O}_4$  are observed, therefore the regeneration of the catalyst is not possible. Characterization by Raman spectroscopy showed the appearance of a band centered at  $694\text{ cm}^{-1}$  (Fig. S3) which corroborates the formation of  $\text{CoTiO}_3$  [74], as evidenced by XRD.

### 3.8.1. Recyclability tests

Stability in reaction is a key property in the development of active and selective heterogeneous catalysts, which also reflects the stability of the catalysts. Recyclability was studied with  $\text{Co}_3\text{O}_4/\text{CeO}_2$  and  $\text{Co}_3\text{O}_4/\text{ZrO}_2$  after calcination at  $400^\circ\text{C}$ , as both showed in the first cycle conversion of glycerol and selectivity toward the target product, lactic acid.

Results are presented in Fig. 9 and gathered in Table S5 with the cobalt loading after every regeneration process.

In the case of  $\text{Co}_3\text{O}_4/\text{CeO}_2$ , it is observed that conversion of glycerol decreases from 77.8 % in the first cycle to 59.5 % in the third cycle with the decrease of cobalt loading from 19.8 to 10.0 wt%, respectively. However, the selectivity towards lactic acid remains stable at  $84.6 \pm 0.9\%$ , thus indicating that active species for directing selectivity towards lactic acid formation are regenerated during regeneration of the catalyst. In the fourth cycle however, conversion and selectivity both fall to values close to the obtained with the bare  $\text{CeO}_2$  and hydrothermal conditions, while the cobalt loading decreased to 7.4 wt%, for instance at such cobalt loading the catalyst no longer shows activity. For  $\text{Co}_3\text{O}_4/\text{ZrO}_2$  catalyst, deactivation of catalyst both, for conversion of glycerol and lactic acid formation, is observed in the second cycle, the conversion went down from 92.5 % with the fresh catalyst to 65.6 % (Table S6), a value lower than the conversion achieved when using the bare  $\text{ZrO}_2$  support as catalyst (76.5 % conversion with  $\text{ZrO}_2$ ); even if the loss of cobalt is comparable with the observed for  $\text{Co}_3\text{O}_4/\text{CeO}_2$  catalyst. The selectivity decrease, being very similar to the selectivity achieved when using  $\text{ZrO}_2$ . The loss in catalytic activity might be attributed not only to the leaching of cobalt, but also to the deposition of carbonaceous deposits that are not completely removed under the calcination conditions (Fig. S2). In the third cycle, a conversion of 47.1 % was achieved, similar to that obtained without the presence of a catalyst (47.6 % conversion), in addition, the selectivity towards lactic acid reached 62.6 %, which is lower than that obtained under hydrothermal reaction conditions (69.2 %) which might be attributed to the degradation of lactic acid leading to carbonaceous deposits formation (Fig. S2 and S3).

These results indicate that  $\text{Co}_3\text{O}_4/\text{CeO}_2$  catalyst exhibits greater performance in terms of selectivity and cyclability, thus  $\text{CeO}_2$  is a more suitable support for  $\text{Co}_3\text{O}_4$  than  $\text{ZrO}_2$  and  $\text{TiO}_2$ .  $\text{Co}_3\text{O}_4/\text{CeO}_2$  catalyst with low density of acidic sites does not generate the formation of carbonaceous deposits as does  $\text{Co}_3\text{O}_4/\text{ZrO}_2$  catalyst, while  $\text{CeO}_2$  support retains more efficiently the active cobalt oxide species compared to  $\text{ZrO}_2$  through the successive catalytic cycles.

## 4. Conclusion

In this paper, it is demonstrated the influence of the support on the catalytic performance of  $\text{Co}_3\text{O}_4$  in the glycerol selective conversion to lactic acid. According to the results,  $\text{ZrO}_2$  and  $\text{CeO}_2$  allowed achieving active catalysts for converting glycerol while yielding lactic acid. However,  $\text{ZrO}_2$  favored lower selectivity to lactic acid and formation of

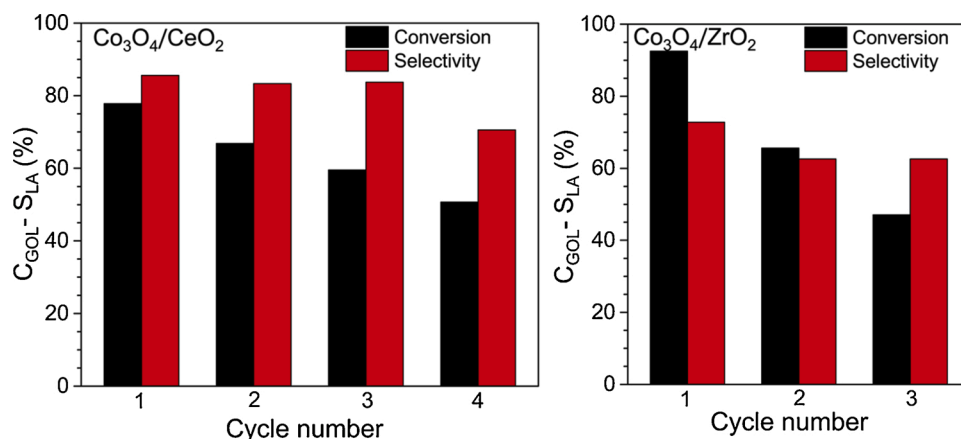


Fig. 9. Catalytic cycles with Co<sub>3</sub>O<sub>4</sub>/CeO<sub>2</sub> and Co<sub>3</sub>O<sub>4</sub>/ZrO<sub>2</sub> catalysts.

carbonaceous species, on the contrary CeO<sub>2</sub> allowed high selectivity to lactic acid avoiding deposition of carbon-containing species and the catalyst could be regenerated for over three catalytic cycles. In this way, the synthesis of a catalyst containing Co<sub>3</sub>O<sub>4</sub> supported on CeO<sub>2</sub> with medium strength acid sites and low concentration of surface cobalt species, mainly enriched in Co<sup>3+</sup> ions being reduced at low temperature, allowed a high degree of conversion of glycerol with high selectivity to lactic acid. On the other hand, TiO<sub>2</sub> is not a suitable support for Co<sub>3</sub>O<sub>4</sub> with the aim of selectively producing lactic acid from glycerol. Although Co<sub>3</sub>O<sub>4</sub>/TiO<sub>2</sub> catalyst exhibited the higher concentration of cobalt species at the surface and a high density of acid sites, glycerol was not activated on this catalyst, perhaps because of the formation of cobalt titanates such as CoTiO<sub>3</sub>, with Co<sup>2+</sup> ions in strong interaction with TiO<sub>2</sub> support.

The results obtained showed the potential of Co<sub>3</sub>O<sub>4</sub>/CeO<sub>2</sub> catalyst for converting alcohols to valuable carboxylic acids as demonstrated with the conversion of glycerol to lactic acid. However, the catalyst exhibited low cyclability mainly because of the leaching of cobalt during reaction. For instance, more studies in cobalt-based heterogeneous catalysts are needed for a profound understanding of activity and stability in alcohol valorization.

#### CRediT authorship contribution statement

**Sebastian Torres:** Methodology, Validation, Investigation, Visualization, Writing - original draft. **Ruben Palacio:** Methodology, Conceptualization, Writing - review & editing, Supervision. **Diana López:** Conceptualization, Writing - review & editing, Supervision, Funding acquisition.

#### Declaration of Competing Interest

The authors declare that they have no known competing financial interests or personal relationships that could have appeared to influence the work reported in this paper.

#### Acknowledgements

To the University of Antioquia, for the academic encouragement of a student instructor to pursue a master's degree in chemical sciences. The authors also thank to the University of Antioquia UdeA.

#### Appendix A. Supplementary data

Supplementary material related to this article can be found, in the online version, at doi:<https://doi.org/10.1016/j.apcata.2021.118199>.

#### References

- [1] H. Zhang, H. Li, C.C. Xu, S. Yang, *ACS Catal.* 9 (2019) 10990–11029.
- [2] Y. Li, W. Shen, *Chem. Soc. Rev.* 43 (2014) 1543–1574.
- [3] G.A. Somorjai, H. Frei, J.Y. Park, *J. Am. Chem. Soc.* 131 (2009) 16589–16605.
- [4] A. Bavykina, N. Kolobov, I.S. Khan, J.A. Bau, A. Ramirez, J. Gascon, *Chem. Rev.* 120 (2020) 8468–8535.
- [5] C. Zhao, Y. Kou, A.A. Lemonidou, X. Li, J.A. Lercher, *Angew. Chem. Int. Ed. Engl.* 48 (2009) 3987–3990.
- [6] A. Bjelić, M. Grilc, M. Huš, B. Likozar, *Chem. Eng. J.* 359 (2019) 305–320.
- [7] M. Alda-Onggar, P. Mäki-Arvela, A. Aho, I.L. Simakova, D.Y. Murzin, *React. Kinet. Mech. Catal.* 126 (2018) 737–759.
- [8] B.N. Zope, D.D. Hibbitts, M. Neurock, R.J. Davis, *Science* 330 (2010) 74.
- [9] J. Xie, P. Duan, N. Kaylor, K. Yin, B. Huang, K. Schmidt-Rohr, R.J. Davis, *ACS Catal.* 7 (2017) 6745–6756.
- [10] J. Ftouni, N. Villandier, F. Auneau, M. Besson, L. Djakovitch, C. Pinel, *Catal. Today* 257 (Part 2) (2015) 267–273.
- [11] E.P. Maris, R.J. Davis, *J. Catal.* 249 (2007) 328–337.
- [12] E.P. Maris, W.C. Ketchie, M. Murayama, R.J. Davis, *J. Catal.* 251 (2007) 281–294.
- [13] S. Oh, H.S. Choi, I.-G. Choi, J.W. Choi, *RSC Adv.* 7 (2017) 15116–15126.
- [14] S. De, J. Zhang, R. Luque, N. Yan, *Energy Environ. Sci.* 9 (2016) 3314–3347.
- [15] B.C. Miranda, R.J. Chimentão, J.B.O. Santos, F. Gispert-Guirado, J. Llorca, F. Medina, F.L. Bonillo, J.E. Sueiras, *Appl. Catal. B* 147 (2014) 464–480.
- [16] A.Z. Abdullah, M.H. Yaacob, N.I. Basir, *J. Ind. Eng. Chem.* 85 (2020) 282–288.
- [17] D. Roy, B. Subramaniam, R.V. Chaudhari, *ACS Catal.* 1 (2011) 548–551.
- [18] G.-Y. Yang, Y.-H. Ke, H.-F. Ren, C.-L. Liu, R.-Z. Yang, W.-S. Dong, *Chem. Eng. J.* 283 (2016) 759–767.
- [19] H. Yin, C. Zhang, H. Yin, D. Gao, L. Shen, A. Wang, *Chem. Eng. J.* 288 (2016) 332–343.
- [20] J. Mazarío, P. Concepción, M. Ventura, M.E. Domine, *J. Catal.* 385 (2020) 160–175.
- [21] M. Wang, J. Ma, H. Liu, N. Luo, Z. Zhao, F. Wang, *ACS Catal.* 8 (2018) 2129–2165.
- [22] A. Corma Canos, S. Iborra, A. Veltj, *Chem. Rev.* 107 (2007) 2411–2502.
- [23] G. Dodekatos, S. Schünemann, H. Tüysüz, *ACS Catal.* 8 (2018) 6301–6333.
- [24] M. Pagliaro, R. Ciriminna, H. Kimura, M. Rossi, C. Della Pina, *Angew. Chem. Int. Ed.* 46 (2007) 4434–4440.
- [25] E. Skrzyńska-Ćwiakalska, M. Capron, F. Dumeignil, *Adv. Sustainable Syst.* (2020), 2000002.
- [26] M. Checa, S. Nogales-Delgado, V. Montes, J.M. Encinar, *Catalysts* 10 (2020).
- [27] G. Innocenti, E. Papadopoulos, G. Fornasari, F. Cavani, A.J. Medford, C. Sievers, *ACS Catal.* 10 (2020) 11936–11950.
- [28] I.Y. Fleitlikh, B.N. Kuznetsov, L.K. Nikiforova, N.A. Grigorjeva, N.G. Beregovtsova, *Ind. Eng. Chem. Res.* 57 (2018) 1331–1336.
- [29] M. Dusselier, P. Van Wouwe, A. Dewaele, E. Makshina, B.F. Sels, *Energy Environ. Sci.* 6 (2013) 1415–1442.
- [30] X. Jin, L. Dang, J. Lohrman, B. Subramaniam, S. Ren, R.V. Chaudhari, *ACS Nano* 7 (2013) 1309–1316.
- [31] X. Deng, G. Dodekatos, K. Pupovac, C. Weidenthaler, W.N. Schmidt, F. Schüth, H. Tüysüz, *ChemCatChem* 7 (2015) 3832–3837.
- [32] Z. Tang, H. Cao, Y. Tao, H.J. Heeres, P.P. Pescarmona, *Appl. Catal. B* 263 (2020) 118273.
- [33] Z. Xiu, H. Wang, C. Cai, C. Li, L. Yan, C. Wang, W. Li, H. Xin, C. Zhu, Q. Zhang, Q. Liu, L. Ma, *Ind. Eng. Chem. Res.* 59 (2020) 9912–9925.
- [34] L. Shen, X. Zhou, A. Wang, H. Yin, H. Yin, W. Cui, *RSC Adv.* 7 (2017) 30725–30739.
- [35] R. Palacio, D. López, D. Hernández, *J. Nanopart. Res.* 21 (2019) 148–160.
- [36] Y. Shen, S. Zhang, H. Li, Y. Ren, H. Liu, *Chem. Eur. J.* 16 (2010) 7368–7371.
- [37] X. Jin, M. Zhao, C. Zeng, W. Yan, Z. Song, P.S. Thapa, B. Subramaniam, R. V. Chaudhari, *ACS Catal.* 6 (2016) 4576–4583.
- [38] R. Palacio, S. Torres, D. Lopez, D. Hernandez, *Catal. Today* 302 (2018) 196–202.
- [39] T. Ahmad, *Adv. Mater. Sci. Eng. Int. J.* 1 (2017) 100–104.

- [40] I. Kartini, P. Meredith, J.C. Diniz da Costa, G.Q. Lu, J. Solgel Sci. Technol. 31 (2004) 185–189.
- [41] L. Lei, Y. Wang, Z. Zhang, J. An, F. Wang, ACS Catal. 10 (2020) 8788–8814.
- [42] L. Lei, Z. Wu, H. Liu, Z. Qin, C. Chen, L. Luo, G. Wang, W. Fan, J. Wang, J. Mater. Chem. A 6 (2018) 9948–9961.
- [43] R. Riva, H. Miessner, R. Vitali, G. Del Piero, Appl. Catal., A 196 (2000) 111–123.
- [44] F. Rouquerol, J. Rouquerol, K.S.W. Sing, G. Maurin, P. Llewellyn, in: F.R.R.S.W.S. L. Maurin (Ed.), Adsorption by Powders and Porous Solids, second edition, Academic Press, Oxford, 2014, pp. 1–24.
- [45] S.C. Petitto, M.A. Langell, J. Vac. Sci. Technol. A 22 (2004) 1690–1696.
- [46] C.A.F. Vaz, D. Prabhakaran, E.I. Altman, V.E. Henrich, Phys. Rev. B 80 (2009), 155457.
- [47] H. Hu, S. Cai, H. Li, L. Huang, L. Shi, D. Zhang, J. Phys. Chem. C 119 (2015) 22924–22933.
- [48] T.E. Davies, T. Garcia, B. Solsona, S.H. Taylor, Chem. Commun. (Camb) (2006) 3417–3419.
- [49] M. Cargnello, C. Gentilini, T. Montini, E. Fonda, S. Mehraeen, M. Chi, M. Herrera-Collado, N.D. Browning, S. Polizzi, L. Pasquato, P. Fornasiero, Chem. Mater. 22 (2010) 4335–4345.
- [50] J. Liu, Z. Zhao, J. Wang, C. Xu, A. Duan, G. Jiang, Q. Yang, Appl. Catal. B 84 (2008) 185–195.
- [51] S. Zhang, X.-S. Li, B. Chen, X. Zhu, C. Shi, A.-M. Zhu, ACS Catal. 4 (2014) 3481–3489.
- [52] H.-X. Mai, L.-D. Sun, Y.-W. Zhang, R. Si, W. Feng, H.-P. Zhang, H.-C. Liu, C.-H. Yan, J. Phys. Chem. 109 (2005) 24380–24385.
- [53] J.M. Pigos, C.J. Brooks, G. Jacobs, B.H. Davis, Appl. Catal. A 319 (2007) 47–57.
- [54] S. Damyanova, B. Pawelec, K. Arishtirova, M.V.M. Huerta, J.L.G. Fierro, Appl. Catal. B 89 (2009) 149–159.
- [55] Y. Okamoto, K. Nagata, T. Adachi, T. Imanaka, K. Inamura, T. Takyu, J. Phys. Chem. 95 (1991) 310–319.
- [56] Y. Li, X. Chen, C. Wang, C. Zhang, H. He, ACS Catal. 8 (2018) 11377–11385.
- [57] D. Wang, J. Huang, F. Liu, X. Xu, X. Fang, J. Liu, Y. Xie, X. Wang, Catal. Today 339 (2020) 220–232.
- [58] R. Riva, H. Miessner, R. Vitali, G. Del Piero, Appl. Catal. A Gen. 196 (2000) 111–123.
- [59] M. Labaki, S. Siffert, J.-F. Lamonier, E.A. Zhilinskaya, A. Aboukais, Appl. Catal. B 43 (2003) 261–271.
- [60] V.O.O. Gonçalves, P.M. de Souza, T. Cabioc'h, V.T. da Silva, F.B. Noronha, F. Richard, Appl. Catal. B 219 (2017) 619–628.
- [61] Y. Zhao, W. Li, M. Zhang, K. Tao, Catal. Commun. 3 (2002) 239–245.
- [62] E.M. Albuquerque, L.E.P. Borges, M.A. Fraga, C. Sievers, ChemCatChem 9 (2017) 2675–2683.
- [63] D.A. Peña, B.S. Uphade, P.G. Smirniotis, J. Catal. 221 (2004) 421–431.
- [64] G. Busca, L. Lietti, G. Ramis, F. Berti, Appl. Catal. B 18 (1998) 1–36.
- [65] G. Li, C. Zhang, Z. Wang, H. Huang, H. Peng, X. Li, Appl. Catal. A Gen. 550 (2018) 67–76.
- [66] F.J. Hisanori Kishida, Zhouyu Zhou, Takehiko Moriya, Heiji Enomotoy, Chem. Lett. 34 (2005) 2.
- [67] Z. Shen, F. Jin, Y. Zhang, A. Kishita, K. Tohji, Effect of Base Catalysts on Hydrothermal Conversion of Glycerin, 2009 3rd International Conference on Bioinformatics and Biomedical Engineering (2009) 1–4.
- [68] L. Shen, Z. Yu, D. Zhang, H. Yin, C. Wang, A. Wang, J. Chem. Technol. Biot. 94 (2019) 204–215.
- [69] R.K.P. Purushothaman, J. van Haveren, D.S. van Es, I. Melián-Cabrera, J. D. Meeldijk, H.J. Heeres, Appl. Catal. B 147 (2014) 92–100.
- [70] S. Kouva, K. Honkala, L. Lefferts, J. Kanervo, Catal. Sci. Technol. 5 (2015) 3473–3490.
- [71] K.-H. Jacob, E. Knözinger, S. Benier, J. Mater. Chem. 3 (1993) 651–657.
- [72] A. Villa, S. Campisi, K.M.H. Mohammed, N. Dimitratos, F. Vindigni, M. Manzoli, W. Jones, M. Bowker, G.J. Hutchings, L. Prati, Catal. Sci. Technol. 5 (2015) 1126–1132.
- [73] R. Palacio, Á.A. Amaya, D. Blach, S. Torres, D. Hernández, D. López, F. Martínez, ChemistrySelect 5 (2020) 7789–7796.
- [74] B. Jongsomjit, C. Sakdamnusun, J.G. Goodwin, P. Praserthdam, Catal. Lett. 94 (2004) 209–215.
- [75] V. Nichele, M. Signoretto, F. Menegazzo, A. Gallo, V. Dal Santo, G. Cruciani, G. Cerrato, Appl. Catal. B 111–112 (2012) 225–232.